

Velocity Dispersion Functions of Pressure-supported Galaxies in EAGLE Simulations with Varying AGN Feedback

Jungwon Choi¹ and Jubee Sohn^{1, 2}

¹ Department of Physics and Astronomy, Seoul National University, 1 Gwanak-ro, Gwanak-gu, Seoul 08826, Republic of Korea
e-mail: jwchoi29912@gmail.com

² SNU Astronomy Research Center, Seoul National University, Seoul 08826, Republic of Korea
e-mail: jubee.sohn@snu.ac.kr

December 5, 2025

ABSTRACT

We investigate the stellar velocity dispersion functions (VDFs) of pressure-supported galaxies in the EAGLE cosmological simulations. The central stellar velocity dispersion is one of the fundamental dynamical tracers of the total mass of galaxy subhalos, alongside luminosity and stellar mass. Because it reflects the gravitational potential, the stellar velocity dispersion is expected to be relatively insensitive to feedback from Active Galactic Nuclei (AGN), a critical process that regulates the connection between other galaxy observables and subhalo mass. To examine the impact of AGN feedback, we analyze the VDFs from five EAGLE simulation runs, each adopting a different AGN feedback model: one "standard", two "enhanced", one "reduced", and one with no AGN feedback. We compute the stellar velocity dispersions of pressure-supported galaxies using member stellar particles, mimicking fiber spectroscopy. The VDFs from the standard and enhanced AGN feedback models show little difference. However, contrary to our initial expectation that the VDF shape would be largely insensitive to AGN feedback, the simulations with reduced and no AGN feedback show a significant excess of high velocity dispersion galaxies ($\sigma_* > 200 \text{ km s}^{-1}$) and a deficit of low dispersion galaxies ($100 < \sigma_* (\text{km s}^{-1}) < 200$), compared to those with standard or enhanced AGN feedback. The presence of high velocity dispersion galaxies in the no-AGN model arises from enhanced central star formation, due to the absence of AGN-driven gas heating or expulsion. Our results demonstrate that the shape of the theoretical VDF is sensitive to the strength of AGN feedback. These predictions offer a theoretical benchmark for future observational studies of the galaxy velocity dispersion function using large-scale spectroscopic surveys.

Key words. Galaxies: abundances – Galaxies: kinematics and dynamics – Galaxies: luminosity function, mass function – Galaxies: elliptical and lenticular, cD – Methods: numerical

1. Introduction

A standard Λ CDM model suggests that the mass concentration of dark matter (DM) determines the structure formation. Within the DM halos, the gravitational interaction between DM and baryonic matter initiates the complicated formation and evolution of galaxies therein. One of the greatest challenges in studying galaxy evolution in DM halos is identifying an observable that connects the underlying DM halos and observable baryonic matter.

The central stellar velocity dispersion of a galaxy is one of the fundamental galaxy observables that connect the galaxy properties and the underlying DM mass. The central velocity dispersion is a kinematic measure determined by the central gravitational potential of galaxies defined by the total mass of galaxy (sub)halos including DM. Stellar velocity dispersions show good correlations with other observables including luminosity or stellar mass (e.g., Faber & Jackson 1976; Djorgovski & Davis 1987; Cappellari et al. 2013). More importantly, various scaling relations based on the stellar velocity dispersion indicate that stellar velocity dispersions are an excellent tracer of the total mass of galaxy subhalos. For example, the stellar velocity dispersions show a tight correlation with the dark matter velocity dispersion or the dark matter mass of subhalos (Wake et al. 2012; van Uitert et al. 2013; Bogdán & Goulding 2015; Zahid et al. 2016, 2018; Sohn et al. 2024b). The observational studies based on strong or weak gravitational lensing also demonstrate that the stellar velocity

dispersion traces the total mass of galaxy subhalos (e.g., Grillo et al. 2008; Auger et al. 2010; Utsumi et al. 2020).

The stellar velocity dispersion has multiple advantages in tracing the total mass of galaxies. First of all, stellar velocity dispersion is relatively straightforward to obtain compared to other mass tracers including galaxy luminosity or stellar mass. These conventional mass tracers, galaxy luminosity or stellar mass, based on photometry are often suffering from the contamination by the line of sight objects or uncertain boundaries of galaxies (e.g., Bernardi et al. 2010, 2013, 2017). The determination of well-defined boundary is critical to measure the photometric mass tracers. However, the velocity dispersion measurement, particularly using fiber spectroscopy, only requires the obtaining spectrum at the central region of galaxies. Thus, the determination of stellar velocity dispersion is insensitive to the complicated photometric procedure. Second, measuring stellar velocity dispersion is less affected by the complicated assumptions on baryonic physics used for measuring other mass tracers. For example, stellar mass measurement has a systematic variation depending on the assumption of the slope of initial mass function (IMF), metallicity, and star formation history (e.g., Conroy et al. 2009). In contrast, these variations in underlying stellar populations have little impact on the velocity dispersion measurements (e.g., Knabel et al. 2025).

One key advantage of using stellar velocity dispersion is that it provides an independent probe of complex baryonic feed-

back processes, particularly feedback from active galactic nuclei (AGN). AGN feedback was introduced to explain the observed deficit of massive galaxies relative to predictions from dark matter-only models of galaxy mass distributions (e.g., Ciotti & Ostriker 1997; Silk & Rees 1998; Menci et al. 2002; Benson et al. 2003; Binney 2004; Silk 2005; Springel et al. 2005; Li & White 2009). In massive galaxies, AGN feedback plays a critical role by heating or expelling cold gas through the activity of central supermassive black holes, thereby suppressing star formation (e.g., Schawinski et al. 2007; Combes 2017) and limiting the growth of stellar mass. The AGN feedback reach out to the ~ 10 kpc and may affect the stellar mass growth within the region (e.g., Zubovas & King 2016; Harrison & Ramos Almeida 2024). This feedback mechanism has been incorporated into cosmological simulations resulting in broad consistency with observed galaxy luminosity and stellar mass distributions (Schaye et al. 2015; Weigel et al. 2016; Pillepich et al. 2018). However, the detailed physical processes driving AGN feedback remain poorly understood (e.g., Wagner et al. 2012; Li et al. 2018), and its influence on stellar kinematics, particularly on the distribution of stellar velocity dispersions, has not been thoroughly explored.

Here, we investigate the stellar velocity dispersion of galaxies in cosmological numerical simulations with various AGN feedback models implemented. We particularly use the stellar mass to velocity dispersion relation and the stellar velocity dispersion function (hereafter, VDF) to examine the impact of AGN feedback on the stellar velocity dispersion. The VDF is a statistical tool that displays the distribution of galaxy stellar velocity dispersions. In observations, several studies measure the VDFs for quiescent galaxies in field (Sheth et al. 2003; Choi et al. 2007; Chae 2010; Montero-Dorta et al. 2017; Sohn et al. 2017b) or in galaxy clusters (Sohn et al. 2017a, 2022) based on large-scale spectroscopic surveys. To provide the theoretical framework for these observed VDF measurements, Sohn et al. (2024a) derive the cluster VDFs are significantly shifted toward the lower velocity dispersion compared to the observed VDFs. They suggest that understanding the origin of the difference in the observed and simulated VDFs can provide an important test for galaxy formation models implemented in cosmological simulations. We specifically examine whether variations in AGN feedback can account for the apparent offset between the observed and simulated VDFs. We also investigate how the shapes of the VDFs change across different AGN feedback models and compare them with the observed VDF to identify which models best reproduce the data.

Our investigation of the role of AGN feedback on galaxy kinematics is distinctive from previous examination based on luminosity or stellar mass distribution because the simulations are not calibrated to match the stellar velocity dispersion distributions. Thus, the investigation of the stellar velocity dispersion distribution provides an independent testbed for testing AGN feedback models based on the statistical distribution of galaxy properties. Choi et al. (2007) explore the impact of AGN feedback on various galaxy properties including the velocity dispersions based on numerical simulations. Our study extends their work based on a much larger sample provided by cosmological simulations with various AGN feedback models.

In Section 2, we introduce the EAGLE simulations with different AGN feedback models we used. In Section 3, we derive the velocity dispersion functions of galaxies in EAGLE simulations. Based on the comparison between VDFs, we investigate the impact of AGN feedback in the velocity and stellar mass distributions of galaxies in Section 4. We conclude our results in Section 5. Throughout the paper, we adopt the Planck cosmo-

logical parameters for EAGLE run cosmology consistent with Planck Collaboration et al. (2014): $\Omega_m = 0.307$, $\Omega_\Lambda = 0.693$, $\Omega_b = 0.048$, and $h = 0.6777$ ($= H_0/(100 \text{ km s}^{-1} \text{ Mpc}^{-1})$).

2. Data

2.1. EAGLE

We use Evolution and Assembly of GaLaxies and their Environments (EAGLE) cosmological simulations (Crain et al. 2015; Schaye et al. 2015; McAlpine et al. 2016) for studying the velocity dispersions of galaxies. EAGLE includes simulations covering various box sizes with various mass resolutions and baryonic physics models. Here, we use the intermediate resolution simulations with the initial baryonic particle mass $m_g = 1.81 \times 10^6 M_\odot$ and a dark matter (DM) particle mass $m_{\text{dm}} = 9.70 \times 10^6 M_\odot$, covering a 50 Mpc box. We use only the $z = 0$ snapshot in this work. Because our primary goal is to compare the shapes of the velocity dispersion functions across different AGN feedback models, a single redshift snapshot is sufficient. Moreover, we compare the velocity dispersions of simulated galaxies with those of observed galaxies at $z < 0.2$. Zahid et al. (2016) showed that the observed scaling relations between stellar velocity dispersion and stellar mass exhibit little to no redshift evolution. Therefore, using simulated galaxies from the $z = 0$ snapshot provides a reasonable basis for comparison with observed galaxies at $z < 0.2$.

We use simulations covering a comoving volume of $(50 \text{ Mpc})^3$ from the suite of EAGLE simulations. We choose this volume because it includes runs implemented with various AGN feedback models (Schaye et al. 2015). RefL0050N0752 (hereafter, EAGLE-50) is the simulation that uses the standard subgrid physics and numerical techniques of the EAGLE simulation (see more details in Schaye et al. 2015). There are four other simulations with different AGN feedback, including C15AGNdT9L0050N0752 (hereafter, EAGLE-eAGN-dT), ViscHiL0050N0752 (hereafter, EAGLE-eAGN-Visc), C15AGNdT8L0050N0752 (hereafter, EAGLE-wAGN), and NoAGNL0050N0752 (hereafter, EAGLE-NoAGN).

There are two parameters that determine the AGN feedback models in EAGLE simulations: ΔT_{AGN} and C_{visc} . The five simulations we use here are based on AGN feedback models with various combinations of ΔT_{AGN} and C_{visc} . ΔT_{AGN} is the temperature increase of the gas during AGN feedback. A larger ΔT_{AGN} indicates a more powerful feedback event. C_{visc} is the parameter related to the viscosity of a subgrid accretion disk (Crain et al. 2015; Rosas-Guevara et al. 2015). The lower C_{visc} indicates a higher disk viscosity by definition. In a simulation with a lower C_{visc} model, the black hole growth and the resulting AGN feedback are delayed.

EAGLE-50 is the reference model with the standard AGN feedback model with $\Delta T_{\text{AGN}} = 10^{8.5} \text{ K}$ and $C_{\text{visc}} = 2\pi$. EAGLE-eAGN-dT and EAGLE-eAGN-Visc are simulations with enhanced AGN feedback models but different parameterizations. EAGLE-eAGN-dT assumes a more energetic AGN feedback with $\Delta T_{\text{AGN}} = 10^9 \text{ K}$, while EAGLE-eAGN-Visc assumes a lower $C_{\text{visc}} = 2\pi \times 10^{-2}$ indicating a higher mass accretion rate of black holes resulting in a faster onset of the AGN feedback. EAGLE-wAGN employs a weaker AGN feedback with $\Delta T_{\text{AGN}} = 10^8 \text{ K}$ compared to the standard EAGLE AGN feedback model. EAGLE-NoAGN assumes an extreme case where no black holes exist. Table 1 summarizes ΔT_{AGN} and C_{visc} for these five simulations.

Figure 1 displays the mass of black holes (M_{BH}) as a function of the stellar mass of their host subhalos (M_*) in four EAGLE

Table 1. Summary of EAGLE simulations used in this study

ID	Simulation ^a	$\Delta T_{\text{AGN}} [K]^b$	C_{visc}^c
EAGLE-50	RefL0050N0752	$10^{8.5}$	2π
EAGLE-eAGN-dT	C15AGNdT9L0050N0752	10^9	2π
EAGLE-eAGN-Visc	ViscHiL0050N0752	$10^{8.5}$	$2\pi \times 10^{-2}$
EAGLE-wAGN	C15AGNdT8L0050N0752	10^8	2π
EAGLE-NoAGN	NoAGNL0050N0752	–	–

Notes. (a) EAGLE reference ID (b) ΔT_{AGN} is the temperature increment of the gas during AGN feedback. (c) C_{visc} is a subgrid parameter related to the viscosity of the accretion disc of subhalo.

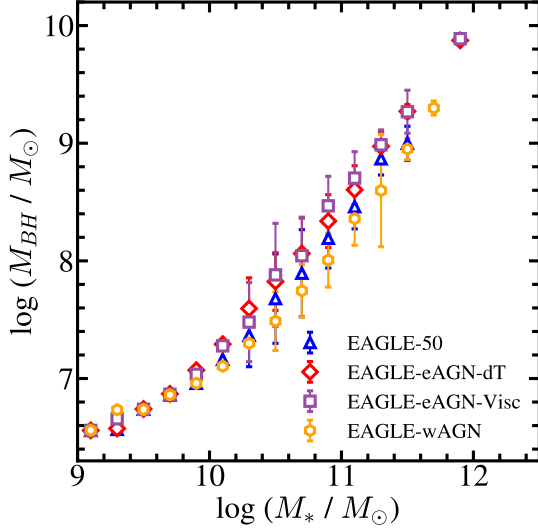


Fig. 1. Median black hole mass as a function of the stellar mass of subhalos in various EAGLE simulations at $z = 0$. Blue triangles, red diamonds, magenta squares, and orange hexagons show the relations from EAGLE-50, EAGLE-eAGN-dT, EAGLE-eAGN-Visc, and EAGLE-wAGN, respectively. At $11.6 < \log(M_*/M_\odot) < 11.8$, EAGLE-50, EAGLE-eAGN-dT, EAGLE-eAGN-Visc do not contain any subhalo in the mass bin; there is no subhalo with $\log(M_*/M_\odot) > 11.9$ in EAGLE-wAGN. Error bars show the 1σ scatter in black hole mass within each stellar mass bin.

simulations (except for EAGLE-NoAGN). The black hole mass (M_{BH}) is directly proportional to the feedback energy injected into the galaxies (Goubert et al. 2024). In general, M_{BH} increases as a function of M_* . The simulations with enhanced AGN feedback models (i.e., EAGLE-eAGN-dT and EAGLE-eAGN-Visc) show a steeper $M_* - M_{\text{BH}}$ relation at $\log(M_*/M_\odot) > 10$. In contrast, the black hole mass in EAGLE-wAGN is lower than those in the other three simulations at fixed stellar mass.

2.2. Identifying Pressure-dominated Subhalos in EAGLE

We use subhalos in EAGLE simulations identified based on the SUBFIND algorithm (Springel et al. 2001; Dolag et al. 2009). We select subhalos with a stellar mass larger than $10^9 M_\odot$, roughly corresponding to the absolute magnitude limits of dense spectroscopic surveys for the low redshift at $0.03 \leq z \leq 0.10$ (Sohn et al. 2017b, 2024b). EAGLE simulations covering a $(50 \text{ Mpc})^3$ volume we use typically contain ~ 1700 subhalos.

We focus on galaxies with pressure-dominated kinematics to study the central stellar velocity dispersions. In the case of rotation-dominated galaxies, the ordered rotation may significantly affect the velocity dispersion measurements (e.g., van

Uitert et al. 2013). We identify pressure-dominated galaxies based on the kinematics of stellar particles of subhalos. In observations, identifying pressure- or rotation-dominated galaxies is not straightforward without spatially resolved spectroscopy. Thus, to facilitate the comparison with the observational sampling of quiescent galaxies, identification of quiescent galaxies based on low specific star formation rate (e.g., Zahid et al. 2016; Sohn et al. 2024b) in simulations is often used.

Unlike previous works, we use the kinematic properties to identify pressure-dominated galaxies because we only compare the simulated properties. Following Dubois et al. (2021), we separate the pressure- and rotation-supported galaxies based on $v/\sigma = 0.5$, where v and σ indicate the rotational velocity and the velocity dispersion of stellar particles.

We derive the rotational velocity (v) based on the angular momentum of stellar particles. To compute v , we first calculate the total angular momentum vector of a galaxy (\mathbf{J}_{tot}) based on the relative positions (\mathbf{x}_i) and relative velocities (\mathbf{v}_i) of stellar particles with respect to the center of the galaxy:

$$\mathbf{J}_{\text{tot}} = \sum_i m_i (\mathbf{x}_i \times \mathbf{v}_i). \quad (1)$$

Then we derive the principal axes ($\hat{\mathbf{J}}_{\text{tot}}$) of the angular momentum:

$$\hat{\mathbf{J}}_{\text{tot}} = \mathbf{J}_{\text{tot}} / |\mathbf{J}_{\text{tot}}|. \quad (2)$$

Here, $\hat{\mathbf{J}}_{\text{tot}}$ corresponds to the galaxy spin axis. Once the galaxy spin axis is defined, we then compute the angular momentum vector of each particle:

$$\mathbf{j}_i = \mathbf{x}_i \times \mathbf{v}_i. \quad (3)$$

The angular momentum ($j_{z,i}$) along with the galaxy spin axis (perpendicular to rotational plane) of each stellar particle is defined as:

$$j_{z,i} = \mathbf{j}_i \cdot \hat{\mathbf{J}}_{\text{tot}}. \quad (4)$$

Additionally, we compute the projected distance on the rotational plane (R_i) of individual stellar particles from the galaxy spin axis. Based on these quantities, we finally compute rotational velocity of galaxies based on stellar particles within the stellar half-mass radius:

$$v = \langle j_{z,i} / R_i \rangle \quad (5)$$

(see also Sales et al. 2010, 2012).

We also compute the stellar velocity dispersion along with the galaxy spin axes we derived from Equation 4. The 1D stellar velocity dispersion is defined as:

$$\sigma = \sqrt{(\sigma_r^2 + \sigma_\theta^2 + \sigma_z^2)/3}. \quad (6)$$

We use the stellar particles within the half-mass radius same as in the rotational velocity. Finally, we compute v/σ of all galaxies based on the definition from Dubois et al. (2021).

Figure 2 shows the v/σ of galaxy subhalos as a function of their stellar mass in the five EAGLE simulations. Black circles in each panel indicate the median v/σ in each stellar mass bin. Horizontal lines mark the boundary separating pressure- and rotation-dominated galaxies.

The $v/\sigma - M_*$ relations vary depending on the AGN feedback models, particularly at $M_* > 10^{10} M_\odot$. Compared to EAGLE-50 with the normal AGN feedback model, the simulations with enhanced AGN feedback models tend to have a smaller number of rotation-dominated galaxies. In contrast, the simulations with weak or no AGN feedback contain a much larger number of rotation-dominated galaxies. The variation of the v/σ relation depending on the AGN feedback model is consistent with the comparison in other simulations: Horizon-AGN versus Horizon-NoAGN (see Figure 3 in Dubois et al. 2016). The differences in the fractions of rotation- and pressure-dominated galaxies suggest that AGN feedback plays a role in determining galaxy kinematics. However, the variation in the $v/\sigma - M_*$ relation across the five EAGLE simulations is less than $\sim 10\%$ in the entire sample of $M_* > 10^9 M_\odot$. Indeed, the $v/\sigma - M_*$ relation changes little at $M_* < 10^{10} M_\odot$. Table 2 summarizes the number of pressure- and rotation-dominated systems in the five simulations.

2.3. Stellar velocity dispersion

We derive the stellar velocity dispersion (σ_*) of pressure-dominated galaxies in the simulations. We also note that the stellar velocity dispersion we derived here differs slightly from the velocity dispersion used to compute v/σ . Following Sohn et al. (2024b) who derive σ_* from IllustrisTNG (see also Sohn et al. 2022, 2024a), we compute the velocity dispersion of member stellar particles of subhalos within a cylindrical volume that penetrates the center of subhalos. We particularly compute the line-of-sight velocity dispersion along with the z -axis, mocking the velocity dispersion measurements based on fiber spectroscopy. We compute the stellar mass-weighted standard deviation as stellar velocity dispersions.

Sohn et al. (2024b) investigate the velocity dispersions based on various definitions in IllustrisTNG, including different viewing axes and measurement techniques. They show that the 1D velocity dispersions measured along the x -, y -, and z -axes are generally consistent to each other. Furthermore, they derive velocity dispersions based on various techniques, including standard deviation, luminosity- or stellar mass-weighted standard deviation, and bi-weight measurements. All velocity dispersion measurements are consistent with each other. Similarly, the velocity dispersion measurements for EAGLE simulations are also insensitive to the various definitions of velocity dispersion. We thus use the stellar mass-weighted standard deviation of stellar particles along with the z -axis as our velocity dispersion measurements (i.e., $\sigma_{*,z}$).

We adopt a fixed 10 kpc aperture to measure stellar velocity dispersions. Using a fixed aperture facilitates comparison with observational measurements, which are typically derived from fiber spectroscopy with fixed angular sizes. Sohn et al. (2024a) and Sohn et al. (2024b) used a 3 kpc fixed aperture to study the stellar velocity dispersions of subhalos in the IllustrisTNG-300 simulation. Here, we employ a slightly larger aperture of 10 kpc, which is sufficiently large to mitigate the effects of gravitational softening in the simulations (i.e., ~ 0.7 kpc for EAGLE simulations, Schaye et al. 2015). Figure 3 shows the relationship between

stellar velocity dispersion measured within 10 kpc ($\sigma_{*,10 \text{ kpc}}$) and stellar mass (M_*) for subhalos in the EAGLE-50 simulation. For comparison, we also show the same relation using velocity dispersions measured within 3 kpc and $R_{h,*}$ apertures (the solid and the dashed lines in Figure 3). The resulting $M_* - \sigma_*$ relations are generally consistent with one another, suggesting that the choice of aperture does not significantly affect the subsequent analysis. Hereafter, we refer to $\sigma_{*,z,10 \text{ kpc}}$ as σ_* .

3. Results

3.1. The $M_* - \sigma_*$ Relations

Figure 4 compares the $M_* - \sigma_*$ relations of five EAGLE simulations. In all five simulations, the stellar velocity dispersion of pressure-dominated galaxies is generally proportional to their stellar mass. The $M_* - \sigma_*$ relations derived from EAGLE simulations with AGN feedback (regardless of the strength) are consistent with each other. However, the $M_* - \sigma_*$ relation from the EAGLE-NoAGN differs from those from the other simulations; the EAGLE-NoAGN velocity dispersions are larger than those in other simulations at a given stellar mass, particularly at $M_* > 10^{10.5} M_\odot$.

Gray solid lines in Figure 4 display the observed $M_* - \sigma_*$ relation from Zahid et al. (2016). The observed relation is derived from quiescent galaxies with D_n4000 larger than 1.5 selected from SDSS spectroscopic sample within $0.02 < z < 0.2$. The observed relation is based on σ_* measured within a 3 kpc aperture. Because the simulated velocity dispersions we compute vary little within 3 kpc and 10 kpc apertures, we compare the observed relation without applying any aperture correction. The observed relation shows a broken power-law with different slopes at $M_* = 10^{10.26} M_\odot$ (see also Nigoche-Netro et al. 2011; Cappellari et al. 2013; Cappellari 2016).

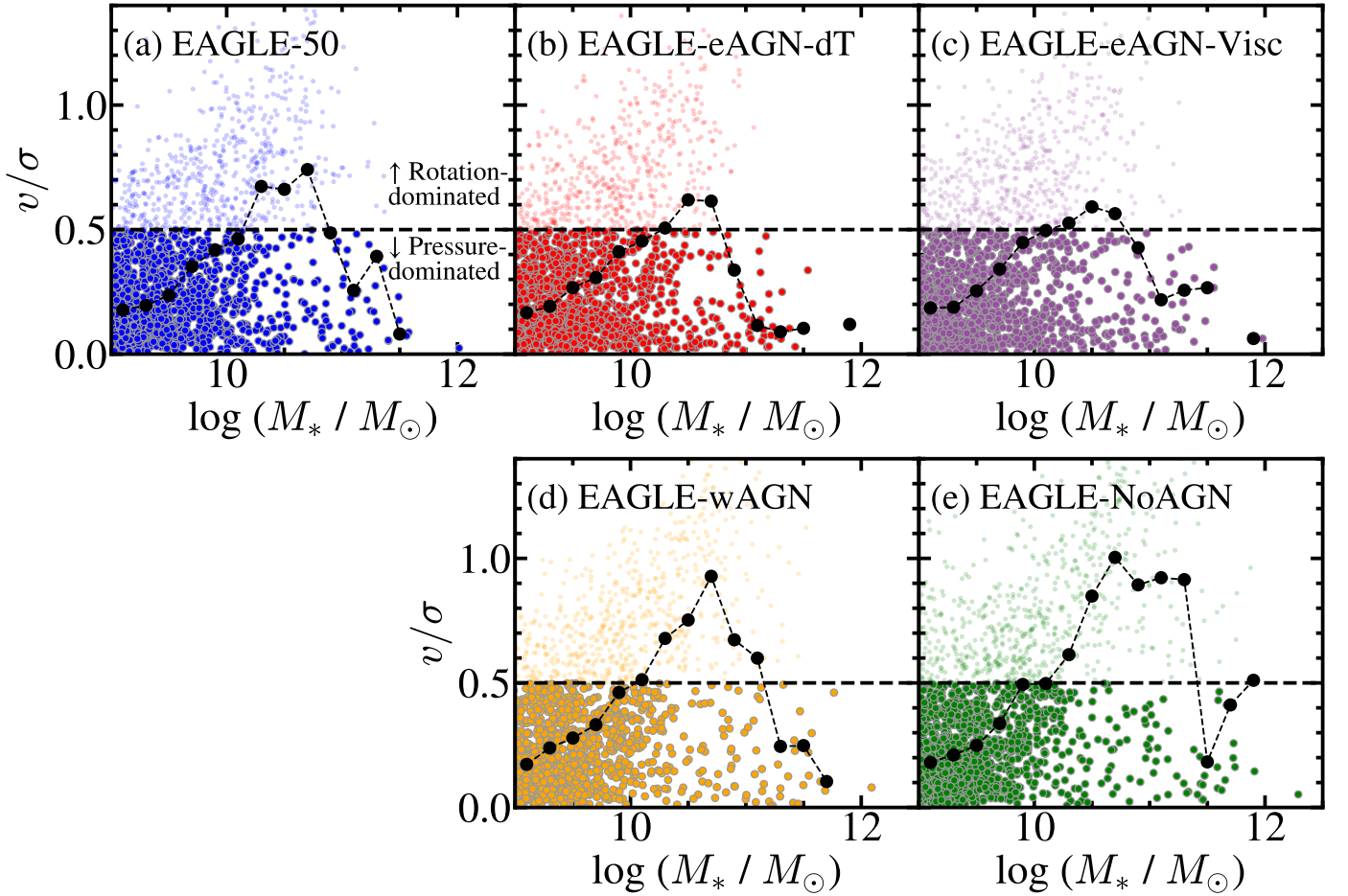
The $M_* - \sigma_*$ relation for EAGLE-NoAGN galaxies is much closer to the observed relation compared to the similar relations for galaxies in other simulations (Figure 4). In particular, galaxies with $M_* > 10^{11} M_\odot$ in EAGLE-NoAGN have comparable velocity dispersions with the observed galaxies. This apparent consistency clearly indicates that the AGN feedback has an impact on the velocity dispersion distributions of galaxies. We discuss the impact of the AGN feedback in Section 4.2.

We also compare the EAGLE $M_* - \sigma_*$ relations with IllustrisTNG-100 (TNG100) simulation. IllustrisTNG simulations use the AGN feedback models implementing the thermal injection (quasar mode) and kinetic wind (kinetic mode) from the AGN (Weinberger et al. 2018; Pillepich et al. 2018), while EAGLE simulations only use the quasar mode (Schaye et al. 2015). We choose TNG100 because the mass resolution of TNG100 is comparable with EAGLE-50 simulations we use. There are TNG50 simulations covering a similar volume with EAGLE-50 simulations, but their mass resolution is an order of magnitude better than the EAGLE-50 simulation. Sohn et al. (2024b) demonstrated that the $M_* - \sigma_*$ relations from TNG50 and TNG100 are offset; the stellar velocity dispersion for TNG50 galaxies are slightly larger than that for TNG100 galaxies at given stellar mass.

We use the TNG100 $M_* - \sigma_{*,z,3 \text{ kpc}}$ relation derived by Sohn et al. (2024b). The TNG100 relation is derived from quiescent galaxies with specific star formation rate lower than $2 \times 10^{-11} \text{ yr}^{-1}$ at $z = 0$. Because Sohn et al. (2024b) showed that the velocity dispersions measured within 3 kpc and 10 kpc are comparable, we use $M_* - \sigma_{*,z,3 \text{ kpc}}$ relation from Sohn et al. (2024b) without any aperture correction.

Table 2. The number of total, pressure- and rotation-dominated galaxies in EAGLE simulations

Simulation	Galaxy selection	$N(M_* > 10^9 M_\odot)$
EAGLE-50	Total	1754
	$v/\sigma < 0.5$	1194
	$v/\sigma \geq 0.5$	560
EAGLE-eAGN-dT	Total	1723
	$v/\sigma < 0.5$	1227
	$v/\sigma \geq 0.5$	496
EAGLE-eAGN-Visc	Total	1714
	$v/\sigma < 0.5$	1197
	$v/\sigma \geq 0.5$	517
EAGLE-wAGN	Total	1707
	$v/\sigma < 0.5$	1110
	$v/\sigma \geq 0.5$	597
EAGLE-NoAGN	Total	1774
	$v/\sigma < 0.5$	1141
	$v/\sigma \geq 0.5$	633

**Fig. 2.** The v/σ ratio as a function of stellar mass for subhalos in (a) EAGLE-50, (b) EAGLE-eAGN-dT, (c) EAGLE-eAGN-Visc, (d) EAGLE-wAGN, and (e) EAGLE-NoAGN. Black circles display the median v/σ as a function of stellar mass for subhalos in each simulation. Horizontal dashed lines indicate $v/\sigma = 0.5$, where the rotation-dominated ($v/\sigma \geq 0.5$) and pressure-dominated ($v/\sigma < 0.5$) galaxies are separated.

In Figure 4, the navy dashed line shows the TNG100 $M_* - \sigma_{*,z,3 \text{ kpc}}$ relation. The TNG100 relation describes the distribution of EAGLE-50 quiescent galaxies very well, except for galaxies in the EAGLE-NoAGN simulation. The relations derived from both simulations differ significantly from the observed relation as Sohn et al. (2024b) already pointed out. In other words,

the $M_* - \sigma_*$ relations derived from EAGLE and TNG100 simulations with AGN feedback are all coincident at $M_* > 10^{10.5} M_\odot$.

3.2. The Velocity Dispersion Complete Samples

The velocity dispersion function (VDF) measures the number of galaxies within bins of velocity dispersion. Deriving the VDF

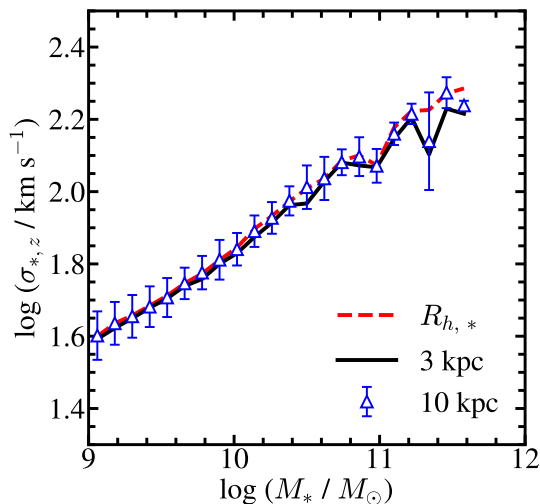


Fig. 3. The median line-of-sight velocity dispersions (along with z -axis) of pressure-dominated galaxies in EAGLE-50 measured within a cylindrical volume with an aperture of 10 kpc (blue triangles). The error bar indicates the 1σ standard deviation in each stellar mass bin. For comparison, the median velocity dispersions are measured within 3 kpc (the black solid line) and the half-mass radius defined by the stellar particles (the red dashed line).

in both observations and simulations can be affected by systematic incompleteness introduced by sample selection. For example, Sohn et al. (2017b) showed that constructing the VDF from a volume-limited sample leads to incompleteness in velocity dispersion, primarily due to the large scatter between velocity dispersion and galaxy magnitude. Similarly, deriving VDFs from simulations also requires care in constructing velocity dispersion-complete samples (Sohn et al. 2024a).

We start constructing the velocity dispersion complete samples from the stellar mass-limited samples (i.e., $M_* > 10^9 M_\odot$) in five EAGLE simulations. Figure 4 displays that stellar velocity dispersions are generally proportional to the stellar mass, but with significant scatters. Because of this scatter, the determination of the velocity dispersion completeness limit of the stellar-mass limited sample is not straightforward.

Following Sohn et al. (2024a), we determine the velocity dispersion completeness limit of the EAGLE stellar mass limited samples (see also Sohn et al. 2017b). We first derive the velocity dispersion boundaries (black dashed lines in Figure 4) where 95% of galaxies in each stellar mass bin are included. We then compute the intercept between the upper 95% boundary and the stellar mass limit (i.e., $M_* = 10^9 M_\odot$). This intercept (horizontal lines in Figure 4) indicates the velocity dispersion limit of the stellar mass-limited sample. In other words, the galaxies with stellar mass lower than the stellar mass limit may have larger velocity dispersion than the velocity dispersion limit. Thus, constructing the VDF based on the stellar mass-limited sample may cause the incompleteness of the VDF below the velocity dispersion completeness limit.

The velocity dispersion completeness limits are $\log \sigma_* \approx 1.7$ across all five simulations. The velocity dispersion completeness limit for EAGLE simulations is consistent with the completeness limit derived from TNG stellar mass limited sample with $\log(M_*/M_\odot) > 9$ ($\log \sigma_* \approx 1.7$; Sohn et al. 2024a). We thus compare the EAGLE and TNG VDFs without concern for differences in completeness. The completeness limits for both EAGLE and TNG are slightly lower than the observed limit ($\log \sigma_* \approx 1.84$) derived from SDSS magnitude- and volume-

limited samples (Sheth et al. 2003; Choi et al. 2007; Sohn et al. 2017b).

The final velocity dispersion complete samples for five EAGLE simulations contain 550–750 pressure-dominated galaxies. We use these velocity dispersion complete samples for our velocity dispersion function measurements in Section 3.3. Table 3 summarizes the number of pressure-dominated galaxy samples in EAGLE simulations we used.

3.3. The Velocity Dispersion Functions in EAGLE simulations

Figure 5 (a) shows the stellar mass functions (SMFs) of pressure-dominated galaxies in the σ_* complete samples for the five EAGLE simulations. We normalize the stellar mass function by the total three-dimensional volume of the simulations. Blue triangles, red diamonds, magenta squares, orange hexagons, and green crosses represent the SMFs for EAGLE-50, EAGLE-eAGN-dT, EAGLE-eAGN-Visc, EAGLE-wAGN, and EAGLE-NoAGN, respectively. Error bars represent Poisson uncertainties. We note that some high stellar mass or stellar velocity dispersion bins contain fewer than 10 galaxies. For these bins, we show only the upper limit, defined as the upper end of the 1σ confidence interval, and omit the lower error bar.

The SMFs from the simulations with normal or enhanced AGN feedback models show consistent stellar mass distributions. The simulations with enhanced AGN feedback models contain slightly fewer massive galaxies as expected, but the difference is insignificant. The SMFs derived from simulations with weak and no AGN feedback are flatter at $10.5 < \log(M_*/M_\odot) < 12$ than the SMFs from simulations with AGN feedback. Massive galaxies with $\log(M_*/M_\odot) > 11$ are more abundant in simulations with no or weak AGN feedback. This comparison indicates that the AGN feedback in EAGLE simulations indeed suppresses the formation of massive galaxies.

In Figure 5 (b), we compare the VDFs measured based on σ_* complete samples for the five EAGLE simulations. Similar to the SMFs, the VDFs from EAGLE-50, EAGLE-eAGN-dT, and EAGLE-eAGN-Visc are consistent with each other. The VDFs from EAGLE-wAGN and EAGLE-NoAGN differ from other VDFs. These simulations with weaker AGN feedback contain significantly more subhalos with $\log \sigma_* > 2.3$. The number of galaxies with $2.0 < \log \sigma_* < 2.3$ in EAGLE-wAGN and EAGLE-NoAGN is relatively lower than in other simulations. We discuss the origin of the differences in VDFs depending on the feedback model in Section 4.2.

3.4. Comparison between simulated & observed VDFs

We next compare the observed and simulated VDFs of pressure-dominated galaxies. We use the observed VDF from Sohn et al. (2017b) constructed from the quiescent galaxies in the SDSS spectroscopy. Sohn et al. (2017b) select quiescent galaxies with $D_n4000 > 1.5$ within the redshift range $0.03 \leq z \leq 0.10$ from SDSS main galaxy sample. They obtain the stellar velocity dispersion measured within a fiducial 3 kpc aperture. Sohn et al. (2017b) demonstrate the importance of building the velocity dispersion complete sample in measuring VDF; they show that the SDSS VDF measured based on the velocity dispersion complete sample is flatter at $\log \sigma_* < 2.1$ compared to the SDSS VDF measured based on the magnitude or volume-limited samples (Sheth et al. 2003; Choi et al. 2007; Chae 2010). We therefore adopt the field VDF from Sohn et al. (2017b), derived from a

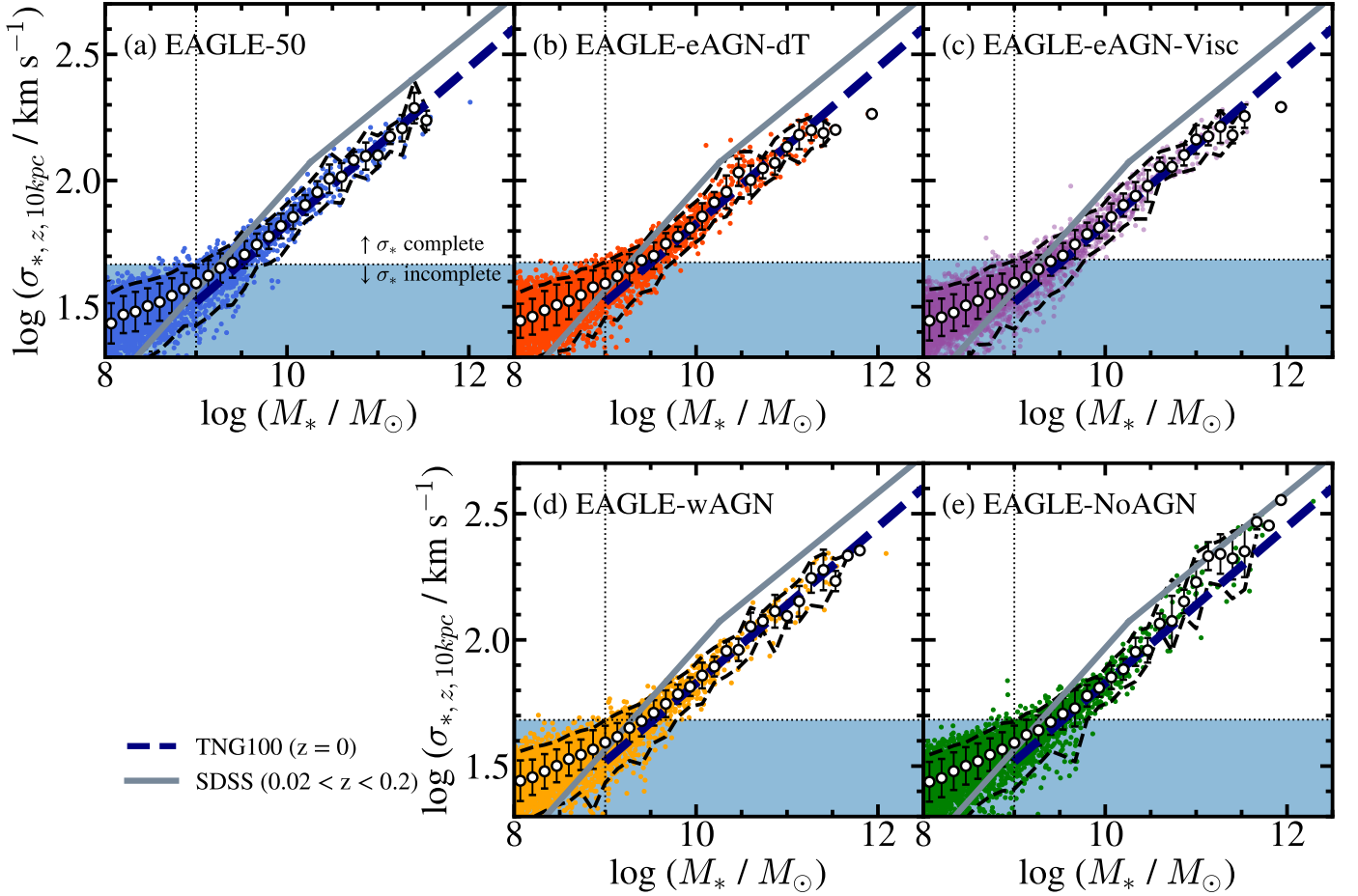


Fig. 4. The stellar mass to 1D stellar velocity dispersion measured within a cylindrical volume with a 10 kpc aperture along with z -axis ($\sigma_{*,z,10\text{ kpc}}$) relations of galaxy subhalos in (a) EAGLE-50, (b) EAGLE-eAGN-dT, (c) EAGLE-eAGN-Visc, (d) EAGLE-wAGN, and (e) EAGLE-NoAGN. White circles show the median $\sigma_{*,z,10\text{ kpc}}$ at each stellar mass bin. Black bold dashed lines show the central 95% of the $\sigma_{*,z,10\text{ kpc}}$ distributions. Vertical dotted lines indicate the stellar mass limit we applied. Horizontal dotted lines mark the velocity dispersion limit where the stellar mass limit intersects with the 95% upper limit of the velocity dispersion distributions. Below this velocity dispersion limit, our EAGLE galaxy samples are incomplete in terms of velocity dispersion. The subhalos in the shaded region are excluded from the σ_* complete sample. The blue dashed lines indicate the $M_* - \sigma_*$ relation for TNG100 (Sohn et al. 2024b), and the gray solid lines show the observed $M_* - \sigma_*$ relation for SDSS quiescent subhalos in the local universe (Zahid et al. 2016).

velocity-dispersion-complete SDSS sample, as it provides the most complete measurement among existing VDF estimates.

Figure 6 (a) compares directly the observed SDSS VDF (the black line and circles) with the VDFs measured from five EAGLE simulations. All five simulated VDFs show significant offsets compared to the observed VDF. The VDF from EAGLE-NoAGN has a comparable value at $\log \sigma_* > 2.4$, but it also deviates from the observed VDF at lower velocity dispersions. The offset between the observed and EAGLE VDFs corresponds to $\Delta \log \sigma_* \sim 0.15 - 0.18$ dex, consistent with the offset in the $M_* - \sigma_*$ relations. The significant offset between observed and EAGLE VDFs is consistent with the result from the comparison between the observed and TNG VDFs (Sohn et al. 2024a).

Figure 6 (b) shows the simulated VDFs after shifting in the σ_* direction, horizontally. To determine the amount of shift, we calculate the mean velocity-dispersion offset between the observed and simulated $M_* - \sigma_*$ relations (see Figure 4) for more than 30 galaxies within $11 < \log(M_*/M_\odot) < 12$. We apply this mean offset when shifting the VDFs to preserve their overall shapes. Interestingly, the shapes of the simulated VDFs from the normal and enhanced AGN feedback are consistent with the shape of the observed VDF. In particular, the slope of the simulated VDFs at

$\log \sigma_* > 2.4$ is consistent with the observed VDF. On the contrary, the VDFs derived from weak or no AGN feedback show a much flatter slope at a high velocity dispersion end.

4. Discussion

We derive the velocity dispersion functions of pressure-dominated galaxies in five EAGLE simulations with various AGN feedback models implemented. The shapes of VDFs measured from these simulations vary; particularly, the VDF measured from EAGLE-NoAGN shows a much flatter slope indicating the relative effective formation of high velocity dispersion galaxies. We also compare these simulated VDFs with the observed VDF. To understand the implications of the differences in VDF shapes, we first examine the impact of sample galaxy selection in Section 4.1. We then discuss the role of AGN feedback to interpret the implication of differences in simulated VDFs in Section 4.2.

4.1. Galaxy Sample Selection

In Figure 6, we show that the EAGLE simulations predict a significantly lower number of galaxies in the velocity dispersion range

Table 3. The number of pressure-dominated galaxies in EAGLE simulations

Simulation	Galaxy selection	$N_{M_*\text{-limited}}^a$	$N_{\sigma_*\text{-limited}}^b$
EAGLE-50	$v/\sigma < 0.5$	1194	728
	$s\text{SFR} < 2 \times 10^{-11} \text{ yr}^{-1}$	554	321
EAGLE-eAGN-dT	$v/\sigma < 0.5$	1227	728
	$s\text{SFR} < 2 \times 10^{-11} \text{ yr}^{-1}$	635	437
EAGLE-eAGN-Visc	$v/\sigma < 0.5$	1197	647
	$s\text{SFR} < 2 \times 10^{-11} \text{ yr}^{-1}$	736	476
EAGLE-wAGN	$v/\sigma < 0.5$	1110	596
	$s\text{SFR} < 2 \times 10^{-11} \text{ yr}^{-1}$	490	283
EAGLE-NoAGN	$v/\sigma < 0.5$	1141	563
	$s\text{SFR} < 2 \times 10^{-11} \text{ yr}^{-1}$	416	200

Notes. ^(a) $N_{M_*\text{-limited}}$ is the number of pressure-dominated galaxies with $M_* > 10^9 M_\odot$. ^(b) $N_{\sigma_*\text{-limited}}$ is the number of pressure-dominated galaxies in the σ_* complete sample defined in each EAGLE simulation (see Section 3).

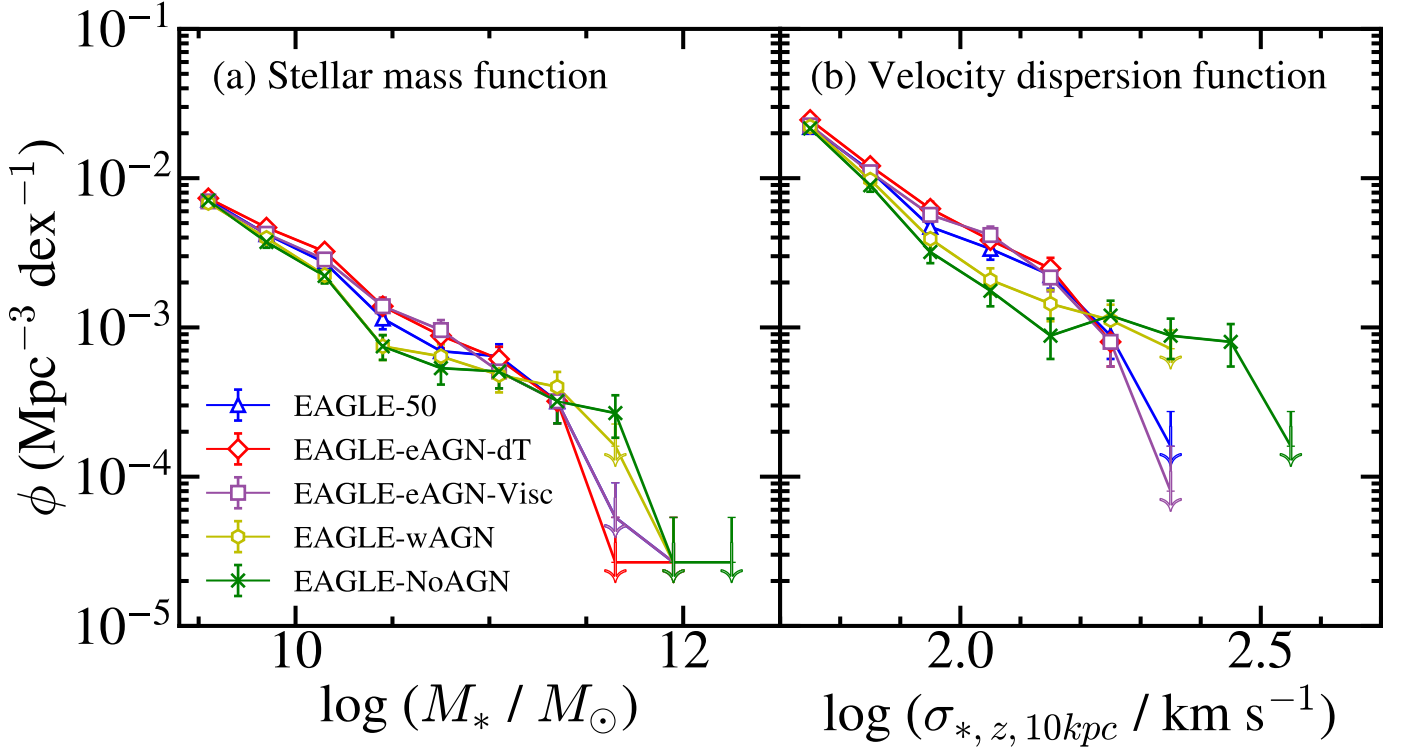


Fig. 5. (a) Stellar mass functions and (b) stellar velocity dispersion functions of pressure-dominated galaxies in five EAGLE simulations. Green crosses show the relations from EAGLE-NoAGN. The other symbols are the same in Figure 1. Error bars indicate Poisson errors. For bins with fewer than 10 galaxies, we display only the upper values, marked by arrows.

$100 < \sigma (\text{km s}^{-1}) < 250$ than the observations. The offset between observed and simulated VDFs is consistent with previous results based on IllustrisTNG simulations (Sohn et al. 2024a). However, we used the different galaxy identification compared to that applied in both observed (Sohn et al. 2017b) and IllustrisTNG galaxy samples (Sohn et al. 2024a). Here, we identify pressure-dominated galaxies based on dynamical properties (i.e., v/σ), which is not straightforward to be applied to observed sample. In contrast, Sohn et al. (2017b) identify quiescent galaxies with $D_n4000 > 1.5$, and Sohn et al. (2024a) select galaxies with specific star formation rate lower than $2 \times 10^{-11} \text{ yr}^{-1}$ in IllustrisTNG300 as quiescent galaxies for their VDF measurements. We thus investigate if the different identification of galaxy samples affects the derivation of VDFs.

Figure 7 shows the specific star formation rate (sSFR) as a function of v/σ for subhalos for $M_* > 10^9 M_\odot$ in the five EAGLE simulations. In Figure 7, galaxies below the horizontal line are classified as quiescent galaxies, identified using the same selection criteria as in Sohn et al. (2024a) (hereafter, the quiescent galaxy sample). Galaxies to the left of the vertical line are pressure-dominated systems (hereafter, the pressure-dominated sample). The overlap between the quiescent and pressure-dominated samples is surprisingly small. Among quiescent galaxies, $\sim 75 - 85 \%$ are pressure-dominated galaxies, whereas only $\sim 30 - 50 \%$ of pressure-dominated galaxies are quiescent galaxies. This difference in sample selection influences the shape of the resulting VDFs.

Figure 8 compares the $M_* - \sigma_*$ relations for the pressure-dominated sample ($v/\sigma < 0.5$, red circles) and the quiescent

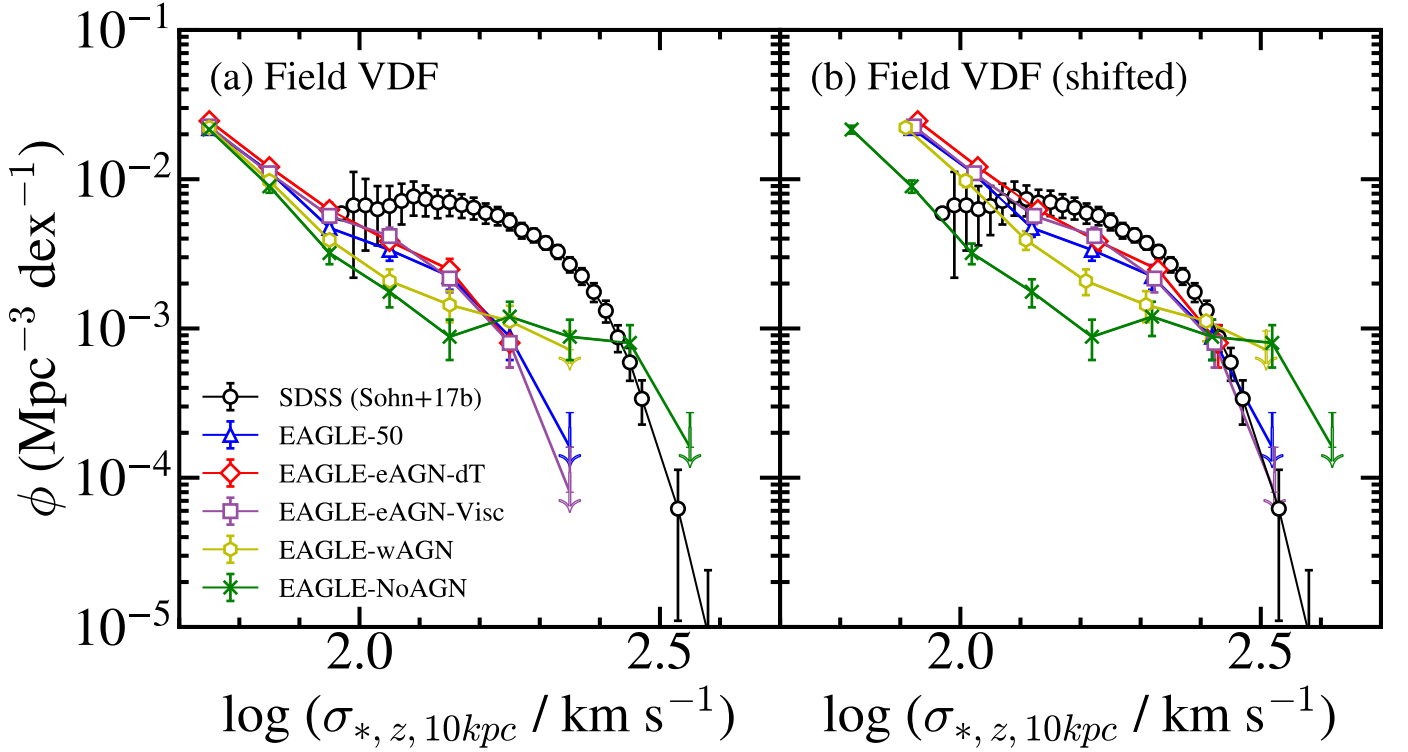


Fig. 6. (a) Comparison between observed and simulated VDFs. Black circles show the observed VDF derived from SDSS field galaxies at $0.03 \leq z \leq 0.10$ (Sohn et al. 2017b). Colored symbols display the simulated VDFs from five EAGLE simulations. Symbols are identical from Figure 5. (b) Same as (a), but the simulated VDFs are shifted by the σ_* offset determined based on the $M_* - \sigma_*$ relations. Error bars on the solid lines indicate Poisson errors. For bins with fewer than 10 galaxies, we display only the upper values, marked by arrows.

sample ($\text{sSFR} < 2 \times 10^{-11} \text{ yr}^{-1}$, blue triangles) in EAGLE-50 simulation. The median $M_* - \sigma_*$ relations for the two samples are consistent over the mass range we explore. In other words, the stellar velocity dispersion does not change significantly at fixed stellar mass, regardless of how galaxies are identified. We also note that the pressure-dominated and the quiescent samples in other EAGLE simulations are also consistent without any offset.

Finally, Figure 9 compares the VDFs derived from two different samples: the quiescent galaxy sample (blue triangles) and the pressure-dominated sample (red circles). The VDFs are generally consistent at $\log \sigma_* > 2.0$, indicating that differences in galaxy classification have minimal impact on the VDF shape at high velocity dispersions. However, at $\log \sigma_* < 2.0$, the VDF from the pressure-dominated sample exhibits a significantly steeper slope than that of the quiescent sample. This steepening is due to the inclusion of many pressure-dominated galaxies with ongoing star formation (i.e., galaxies in the upper left region of Figure 7). More importantly, our analysis indicates that differences in sample selection alone cannot account for the substantial discrepancy between the observed and simulated VDFs, regardless of the adopted AGN feedback model.

4.2. The Role of AGN Feedback in Velocity Dispersion

Our tests imply two important aspects of the VDFs derived from EAGLE simulations with various AGN feedback models. First, the VDFs derived from EAGLE simulations are significantly offset from the observed VDFs, similar to the VDFs derived from other simulations including TNG100 and TNG300 (Sohn et al. 2024a). Second, the $M_* - \sigma_*$ relation and the VDF vary little among EAGLE simulations, except for the one with no AGN feedback model. The steeper $M_* - \sigma_*$ relation of the galaxies in

the EAGLE-NoAGN simulation is intriguing because the detailed physical mechanism of the AGN feedback affecting the stellar kinematics is unclear.

To understand the role of AGN feedback on the stellar kinematics, we examine the origin of the peculiarities in the $M_* - \sigma_*$ relation and the VDF from EAGLE-NoAGN simulation. Unlike the $M_* - \sigma_*$ relation we show in Figure 4, we now investigate the stellar mass to σ_* relation, but based on the M_* measured within 10 kpc aperture (i.e., $M_{*,z,10 \text{ kpc}}$).

In Figure 10, the $M_{*,10 \text{ kpc}} - \sigma_{*,10 \text{ kpc}}$ relations derived from three simulations (i.e., EAGLE-50, EAGLE-eAGN-dT, and EAGLE-NoAGN) do not differ from each other, unlike the $M_* - \sigma_{*,z,10 \text{ kpc}}$ relations shown in Figure 4. The discrepancy between the $M_* - \sigma_{*,z,10 \text{ kpc}}$ and $M_{*,z,10 \text{ kpc}} - \sigma_{*,z,10 \text{ kpc}}$ relations indicates that 1) the stellar velocity dispersion is directly proportional to the stellar mass within the aperture we measure the velocity dispersion and 2) the stellar mass distribution within galaxies varies depending on the AGN feedback models (resulting in the different slopes in $M_* - \sigma_{*,z,10 \text{ kpc}}$ relations). Figure 11 shows that the mass concentration of simulated galaxies varies depending on the adopted AGN feedback model. For $\log M_* < 10.5$, the galaxies in the EAGLE-NoAGN (the green line) continue to follow a proportional relation with M_* , whereas galaxies in the other EAGLE simulations show systematically lower $\log M_{*,z,10 \text{ kpc}}$, reflecting reduced mass concentrations within 10 kpc due to AGN feedback.

Several physical mechanisms contribute to variations in the stellar mass distribution within galaxies (e.g., Furlong et al. 2017; Choi et al. 2018). First, galaxies naturally lose stellar mass as old stars through supernova explosions or during the asymptotic giant branch (AGB) phase. Second, stellar mass redistribution occurs through mergers or interactions between galaxies. These

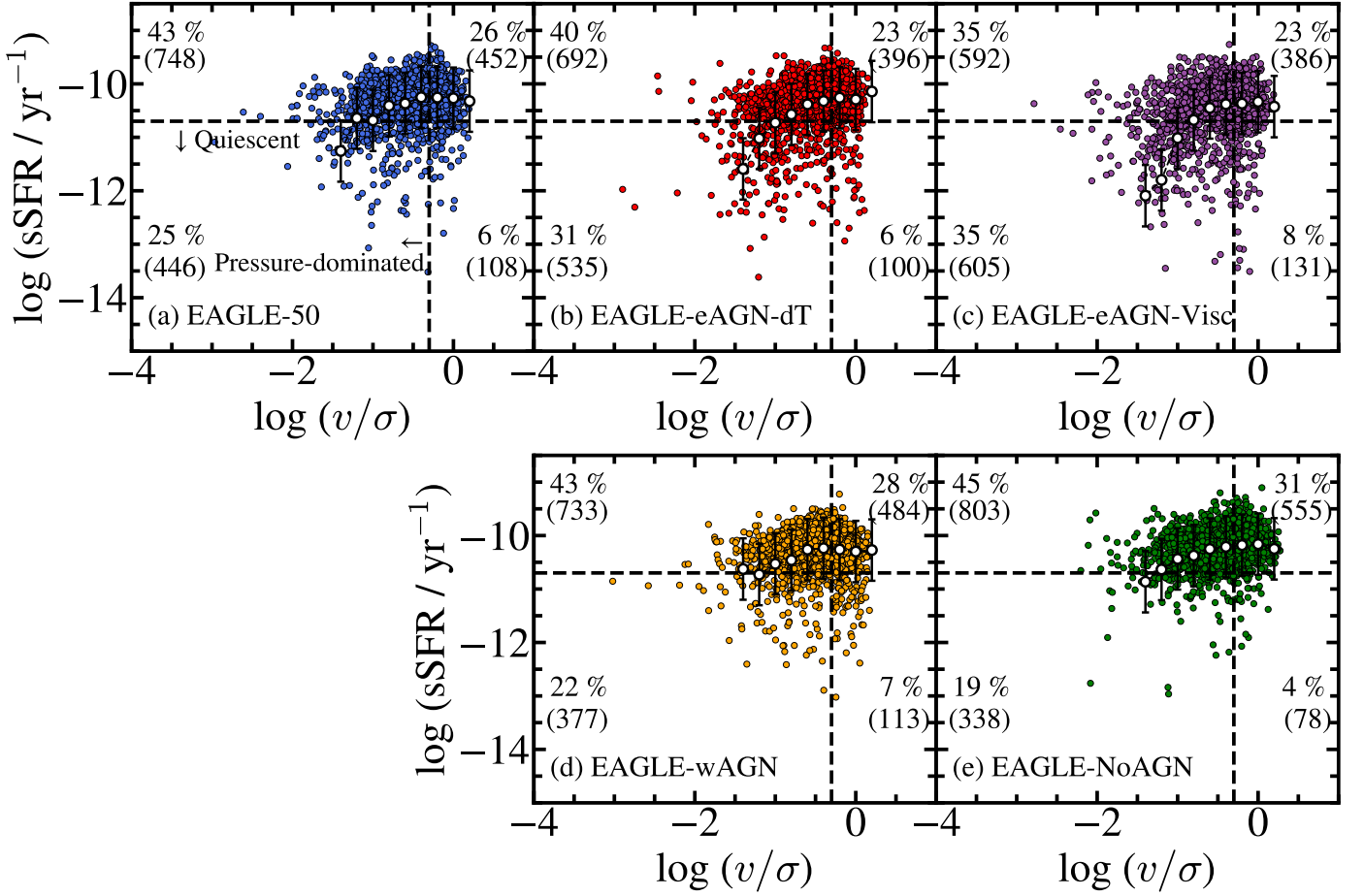


Fig. 7. The specific star formation rate as a function of v/σ for all subhalos in five EAGLE simulations. Vertical lines show the selection boundary between pressure-dominated and rotation-dominated galaxies (i.e., $v/\sigma = 0.5$). Horizontal lines show another boundary that separates quiescent and star-forming galaxies (i.e., $sSFR = 2 \times 10^{-11} \text{ yr}^{-1}$). The numbers indicate the fraction of galaxies in each area among the entire sample with $\log(M_*/M_\odot) > 9$. White circles show the median sSFR at each v/σ bin. The error bar indicates the 1σ standard deviation of the galaxies in each v/σ bin.

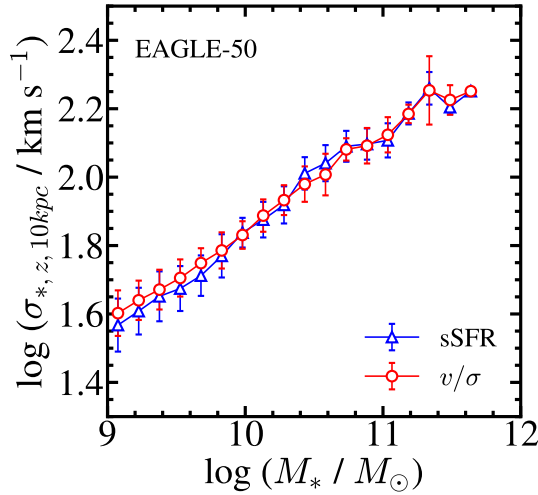


Fig. 8. The median $M_* - \sigma_*$ relation for EAGLE-50. Red circles and blue triangles show the relations derived from pressure-dominated galaxies with $v/\sigma < 0.5$ and the quiescent galaxies with $sSFR < 2 \times 10^{-11} \text{ yr}^{-1}$, respectively. The error bars indicate the 1σ standard deviations.

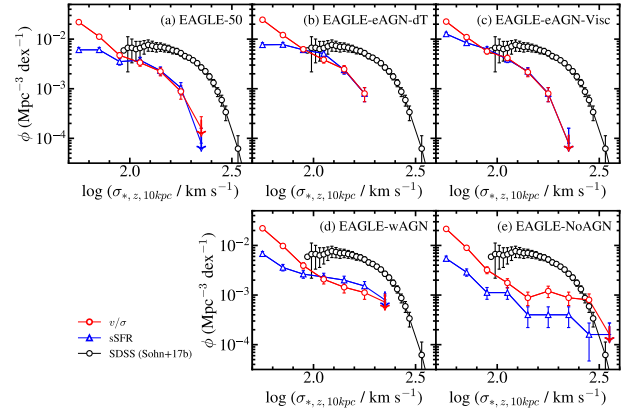


Fig. 9. Comparison between VDFs constructed based on galaxy samples identified based on the v/σ and the sSFR selections in five EAGLE simulations. Black circles show the observed VDF derived from SDSS field galaxies at $0.03 \leq z \leq 0.10$ (Sohn et al. 2017b). Symbols are identical from Figure 8. Error bars on the solid lines indicate Poisson errors. We display only the upper values with arrows for bins including fewer than 10 galaxies.

two processes likely operate to a similar extent regardless of the AGN feedback model employed.

The AGN feedback can change the stellar mass distribution by disturbing the gravitational potential (e.g., Choi et al. 2018).

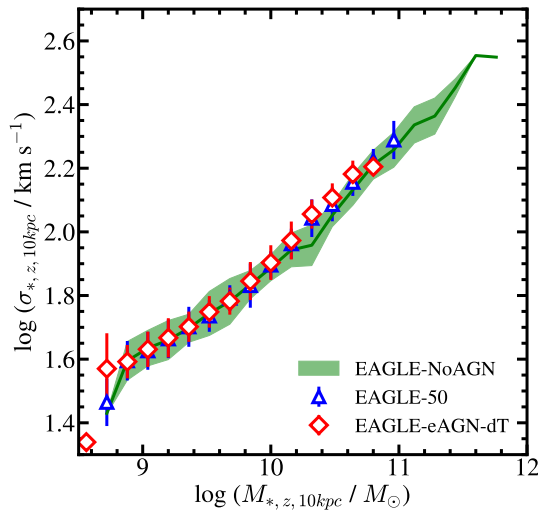


Fig. 10. The median stellar velocity dispersions measured within a cylindrical volume within a 10 kpc aperture as a function of the stellar mass measured within a 10 kpc aperture for pressure-dominated galaxies in various EAGLE simulations at $z = 0$. Blue triangles, red diamonds, and green solid line show the relations from EAGLE-50, EAGLE-eAGN-dT, and EAGLE-NoAGN, respectively. The error bar and shaded region indicate the 1σ standard deviation of the galaxies in each stellar mass bin.

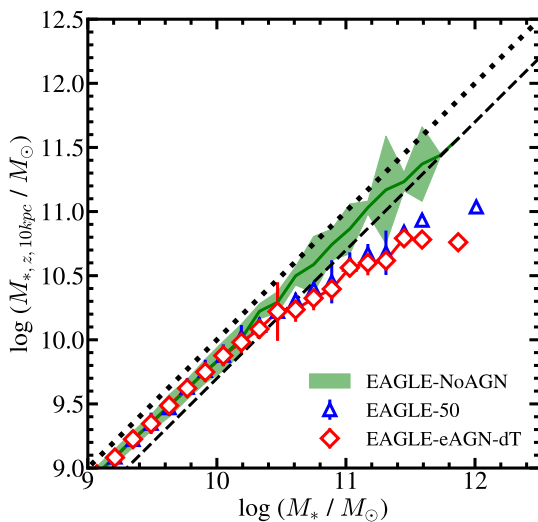


Fig. 11. The median stellar mass measured within a cylindrical volume with a 10 kpc aperture as a function of the total stellar mass of pressure-dominated galaxies in various EAGLE simulations. Symbols are the same in Figure 10. The dashed line indicates the relations between total stellar mass and the stellar mass within half-mass radius. The dotted line indicates the one-to-one correspondence between the two stellar masses. The error bar and shaded region indicate the 1σ standard deviation of the galaxies in each stellar mass bin.

When AGN feedback expels gas from galaxy centers, it reduces the central gravitational potential, causing the inner regions of galaxies to ‘puff up’. As a result, both the stellar and dark matter distributions expand, and the central potential becomes shallower (adiabatic expansion, e.g., Hopkins & Quataert 2010; Fan et al. 2008, 2010). This ‘puff up’ process generally increases the size of galaxies due to the migration of stars (Furlong et al. 2017; Choi et al. 2018). Galaxies in simulations with no AGN feedback then are compact compared to their counterparts in simulations with AGN feedback. Indeed, galaxies in EAGLE-NoAGN are

generally more compact than those in other EAGLE simulations that include AGN feedback, at a fixed stellar mass. In the EAGLE-NoAGN simulation, galaxies with $M_* > 10^{11} M_\odot$ have median half-mass radii of 3–30 kpc, whereas galaxies with similar stellar masses in the other EAGLE simulations are much larger (10 – 130 kpc), with median sizes about four times greater.

Figure 12 shows that the increase in stellar mass in the central region is strongly affected by AGN feedback. Figure 12 (a) shows the change of stellar mass within a 10 kpc aperture as a function of time. We plot the median variation of stellar mass of pressure-dominated galaxies at $z < 1$ in five EAGLE simulations. In general, galaxies in all EAGLE simulations show continuous mass growth at < 10 kpc. However, the median stellar mass growth rate varies significantly depending on the AGN feedback models. The mass growth rate of galaxies simulated with the AGN feedback is generally decreasing as a function of time. In contrast, the mass growth rate of galaxies in EAGLE-NoAGN exhibits a monotonic increase across the redshift range we explore.

Figure 12 (b) displays the resulting stellar mass growth at $z < 1$. Galaxies in EAGLE-NoAGN show a significant mass growth compared to galaxies in other EAGLE simulations. The significant growth of stellar mass within 10 kpc in EAGLE-NoAGN results in excess of $\sigma_{*,z,10\text{ kpc}}$ appeared in the $M_* - \sigma_{*,z,10\text{ kpc}}$ relation and the VDF.

The most significant change in the stellar mass distribution due to the AGN feedback results from the variation in the star formation rate. Figure 13 (a) displays the median specific star formation rate (sSFR) of pressure-dominated galaxies in EAGLE simulations. We note that the specific star formation rate is measured within a spherical 10 kpc aperture for the galaxies, instead of the cylindrical aperture as we examined for Figure 12. The median specific star formation rate (sSFR) of galaxies in EAGLE-NoAGN is higher than that of galaxies in other EAGLE simulations. Overall, the sSFR of galaxies decreases over time, but the sSFR of galaxies in EAGLE-NoAGN decreases relatively slowly than for galaxies in other EAGLE simulations.

Figure 13 (b) compares the amount of stellar mass within a 10 kpc spherical aperture increased by in-situ star formation (i.e., $M_{*,\text{SF},10\text{ kpc}}$) at each redshift. To compute the in-situ stellar mass increment, we simply assume a linear variation of the star formation rate of galaxies between each redshift, then we compute the mass of newly formed stars in between the snapshots. The median $M_{*,\text{SF},10\text{ kpc}}$ of galaxies in EAGLE-NoAGN remains constant at $z < 1$, while the median $M_{*,\text{SF},10\text{ kpc}}$ of galaxies in other EAGLE simulations continuously decrease over time. The decrease in $M_{*,\text{SF},10\text{ kpc}}$ observed in most EAGLE simulations is clearly a result of the reduced availability of cool gas due to AGN feedback.

Additionally, we examine the ex situ stellar mass growth within a 10 kpc aperture. In the four EAGLE simulations that include AGN feedback, the ex situ mass growth is typically an order of magnitude larger than the in situ mass growth. In contrast, galaxies in the EAGLE-NoAGN simulation show comparable in situ and ex situ mass growth at $z < 1$. This indicates that the absence of AGN feedback leads to substantial stellar mass growth from internal star formation in the central region, comparable to that driven by mergers or accretion.

Figure 12 and Figure 13 illustrate the different stellar mass evolution and evolution of stellar mass distribution of galaxies in EAGLE simulations with various AGN feedback models. In general, galaxies in all EAGLE simulations show stellar mass growth at $z < 1$ in the central region. The growth rate varies depending on the implemented AGN feedback model; the galaxies in EAGLE-NoAGN show much significant mass growth in

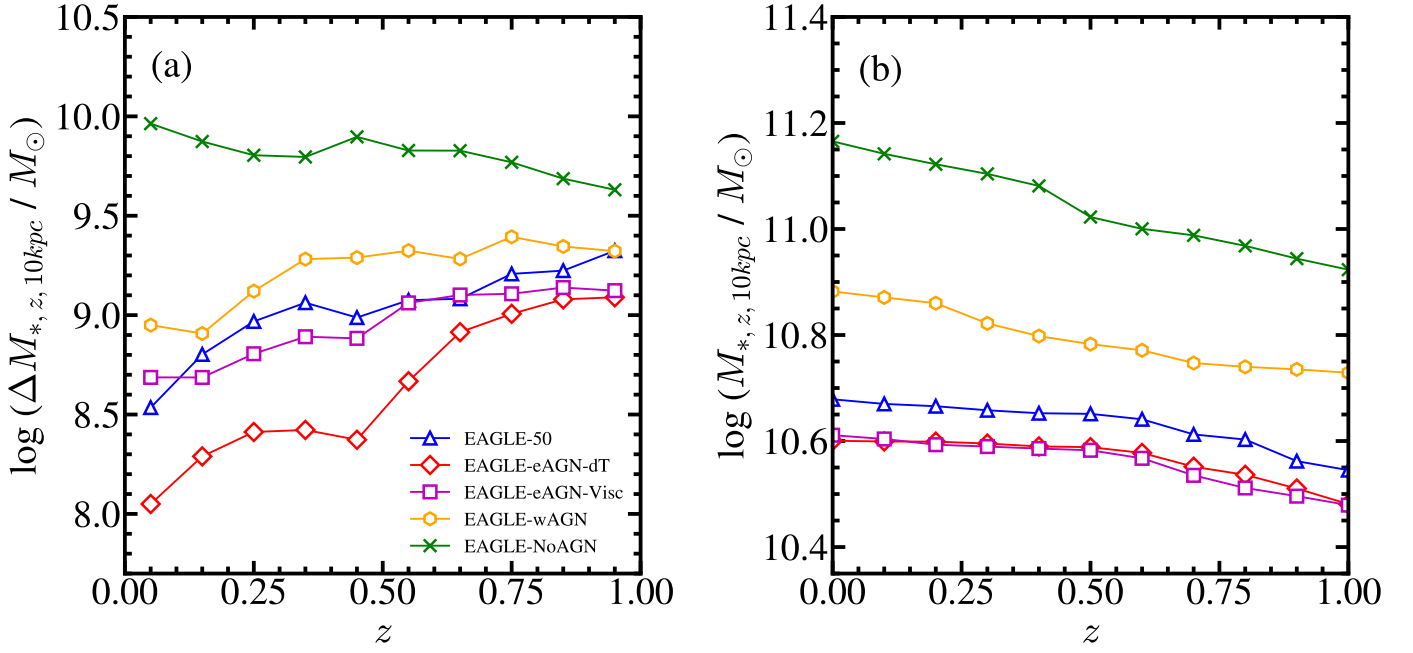


Fig. 12. (a) The median change of $M_{*,z,10\text{ kpc}}$ and (b) The median of $M_{*,z,10\text{ kpc}}$ as a function of redshift in various EAGLE simulations at $z < 1$. The symbols are the same in Figure 5.

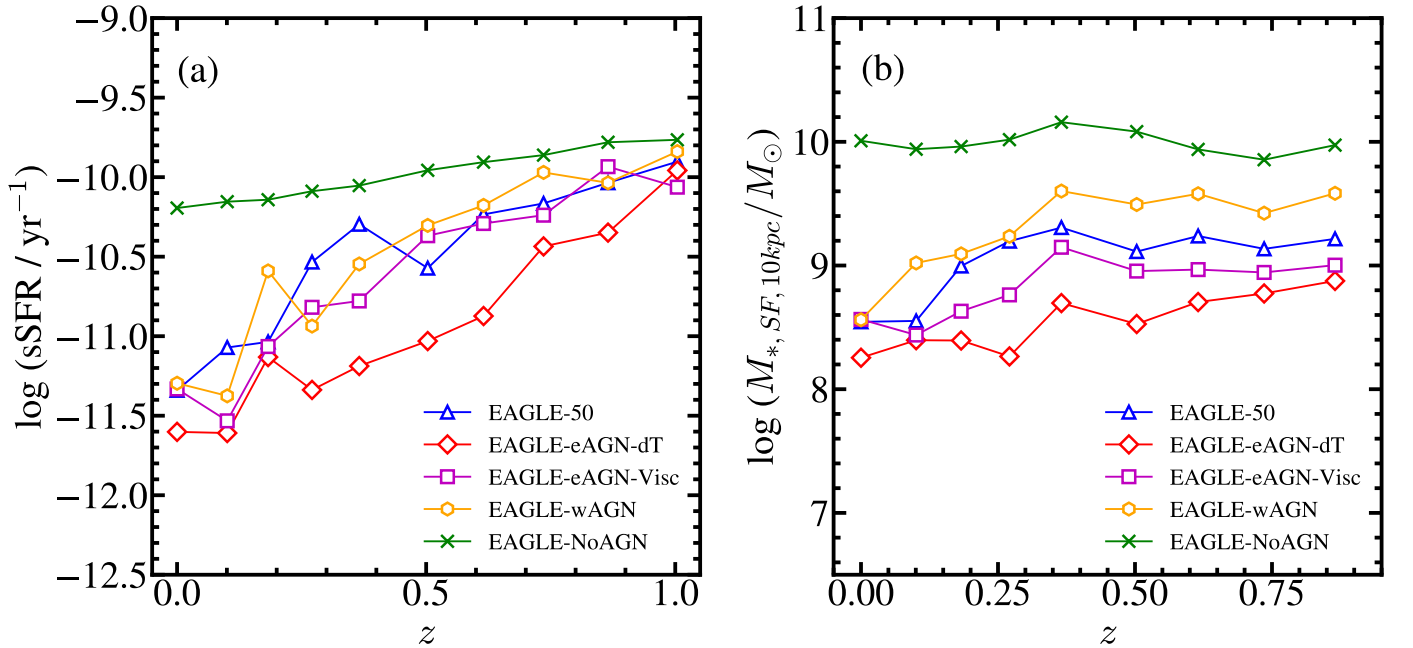


Fig. 13. (a) The median sSFR within a spherical 10 kpc aperture in the five EAGLE simulations as a function of redshift. (b) The median $M_{*,SF,10\text{ kpc}}$, the amount of stellar mass within a 10 kpc spherical aperture increased by in-situ star formation, in various EAGLE simulations as a function of redshift at $z < 1$. The symbols are the same in Figure 5.

the central region. When the AGN feedback is implemented, the central black hole activity suppresses star formation in the central region by heating the gas and expulsion of gas. As a result, the stellar mass growth in the central region is suppressed, in turn, the central stellar velocity dispersions that are proportional to the mass within the central region do not increase significantly. The difference between $M_* - \sigma_{*,z,10\text{ kpc}}$ relations and the VDFs derived from various EAGLE simulations originates from the different star formation history in the central region.

5. Conclusion

We explore the role of AGN feedback on the stellar kinematics of galaxies based on EAGLE simulations with various AGN feedback models. Our analysis is based on five EAGLE runs—EAGLE-50, EAGLE-eAGN-dT, EAGLE-eAGN-Visc, EAGLE-wAGN, and EAGLE-NoAGN—each covering a cubic volume of $(50\text{ Mpc})^3$. We select pressure-dominated galaxies based on stellar kinematics ($v/\sigma < 0.5$) for $\log(M_*/M_{\odot}) > 9$. Furthermore, we construct the velocity dispersion complete sam-

ple in five EAGLE simulations. We then measure stellar velocity dispersions using the same approach we applied for fiber spectroscopy.

The stellar mass–velocity dispersion relations derived from the EAGLE simulations show a significant offset compared to observations: simulated galaxies exhibit systematically lower velocity dispersions at fixed stellar mass. This trend is consistent with results from other cosmological simulations, including IllustrisTNG-100 and 300 (Sohn et al. 2024b). As a result, the velocity dispersion functions (VDFs) derived from all five EAGLE runs are significantly lower than the observed VDF.

Despite the systematic offset, comparing the stellar velocity dispersions across EAGLE models with different AGN feedback implementations reveals the impact of AGN feedback on stellar kinematics. The VDF from EAGLE-NoAGN shows a substantial excess of high velocity dispersion galaxies ($\log \sigma_* > 2.3$) and a flatter slope at $\log \sigma_* > 2.0$ relative to those from other EAGLE simulations. This discrepancy strongly suggests that the AGN feedback is certainly responsible for the stellar velocity dispersion (and the underlying mass) distribution of galaxies.

In order to investigate the physical mechanisms of AGN feedback that affect the stellar kinematics, we investigate the $M_* - \sigma_*$ scaling relations measured within a fixed 10 kpc aperture in EAGLE simulations. The $M_* - \sigma_*$ relations in all EAGLE simulations have essentially identical shapes that velocity dispersions are simply proportional to the stellar mass enclosed in the aperture we use for measuring velocity dispersion. In other words, the discrepancy in the VDFs results from the underlying mass distribution rather than any peculiarity in the scaling relation between mass and stellar kinematics.

We further show that stellar mass concentration varies significantly with AGN feedback. Galaxies in EAGLE-NoAGN display much stronger central mass concentrations (within 10 kpc) than their counterparts in the other runs. This is primarily driven by sustained central star formation in the absence of AGN feedback, as opposed to the suppressed central star formation seen in simulations with AGN. These differences in stellar mass concentration naturally propagate to differences in stellar velocity dispersions.

The VDF offers a promising probe of the dark matter (DM) subhalo mass function (Sohn et al. 2017b, 2024a). Prior studies (Zahid et al. 2018; Sohn et al. 2024b) have highlighted a tight correlation between stellar velocity dispersion and the velocity dispersion of the host DM halo. As a next step, comparing the DM mass functions and DM VDFs from simulations will help place further constraints on the stellar VDF as a tracer of the underlying dark matter distribution.

Acknowledgements. We acknowledge the Virgo Consortium for making their simulation data available. The EAGLE simulations were performed using the DiRAC-2 facility at Durham, managed by the ICC, and the PRACE facility Curie based in France at TGCC, CEA, Bruyères-le-Châtel. J.S. is supported by the National Research Foundation of Korea (NRF) grant funded by the Korean government (MSIT) (RS-2023-00210597). This work was also supported by the Global-LAMP Program of the National Research Foundation of Korea (NRF) grant funded by the Ministry of Education (No. RS-2023-00301976).

References

Auger, M. W., Treu, T., Bolton, A. S., et al. 2010, *ApJ*, 724, 511
 Benson, A. J., Bower, R. G., Frenk, C. S., et al. 2003, *ApJ*, 599, 38
 Bernardi, M., Meert, A., Sheth, R. K., et al. 2017, *MNRAS*, 467, 2217
 Bernardi, M., Meert, A., Sheth, R. K., et al. 2013, *MNRAS*, 436, 697
 Bernardi, M., Shankar, F., Hyde, J. B., et al. 2010, *MNRAS*, 404, 2087
 Binney, J. 2004, *MNRAS*, 347, 1093
 Bogdán, Á. & Goulding, A. D. 2015, *ApJ*, 800, 124
 Cappellari, M. 2016, *ARA&A*, 54, 597
 Cappellari, M., Scott, N., Alatalo, K., et al. 2013, *MNRAS*, 432, 1709

Chae, K.-H. 2010, *MNRAS*, 402, 2031
 Choi, E., Somerville, R. S., Ostriker, J. P., Naab, T., & Hirschmann, M. 2018, *ApJ*, 866, 91
 Choi, Y.-Y., Park, C., & Vogeley, M. S. 2007, *ApJ*, 658, 884
 Ciotti, L. & Ostriker, J. P. 1997, *ApJ*, 487, L105
 Combes, F. 2017, in *Quasars at all Cosmic Epochs*, 20
 Conroy, C., Gunn, J. E., & White, M. 2009, *ApJ*, 699, 486
 Crain, R. A., Schaye, J., Bower, R. G., et al. 2015, *MNRAS*, 450, 1937
 Djorgovski, S. & Davis, M. 1987, *ApJ*, 313, 59
 Dolag, K., Borgani, S., Murante, G., & Springel, V. 2009, *MNRAS*, 399, 497
 Dubois, Y., Beckmann, R., Bournaud, F., et al. 2021, *A&A*, 651, A109
 Dubois, Y., Peirani, S., Pichon, C., et al. 2016, *MNRAS*, 463, 3948
 Faber, S. M. & Jackson, R. E. 1976, *ApJ*, 204, 668
 Fan, L., Lapi, A., Bressan, A., et al. 2010, *ApJ*, 718, 1460
 Fan, L., Lapi, A., De Zotti, G., & Danese, L. 2008, *ApJ*, 689, L101
 Furlong, M., Bower, R. G., Crain, R. A., et al. 2017, *MNRAS*, 465, 722
 Goubert, P. H., Bluck, A. F. L., Piotrowska, J. M., & Maiolino, R. 2024, *MNRAS*, 528, 4891
 Grillo, C., Lombardi, M., & Bertin, G. 2008, *A&A*, 477, 397
 Harrison, C. M. & Ramos Almeida, C. 2024, *Galaxies*, 12, 17
 Hopkins, P. F. & Quataert, E. 2010, *MNRAS*, 407, 1529
 Knabel, S., Mozumdar, P., Shajib, A. J., et al. 2025, *arXiv e-prints*, arXiv:2502.16034
 Li, C. & White, S. D. M. 2009, *MNRAS*, 398, 2177
 Li, Y.-P., Yuan, F., Mo, H., et al. 2018, *ApJ*, 866, 70
 McAlpine, S., Helly, J. C., Schaller, M., et al. 2016, *Astronomy and Computing*, 15, 72
 Menci, N., Cavaliere, A., Fontana, A., Giallongo, E., & Poli, F. 2002, *ApJ*, 575, 18
 Montero-Dorta, A. D., Bolton, A. S., & Shu, Y. 2017, *MNRAS*, 468, 47
 Nigoche-Netro, A., Aguerri, J. A. L., Lagos, P., et al. 2011, *A&A*, 534, A61
 Pillepich, A., Springel, V., Nelson, D., et al. 2018, *MNRAS*, 473, 4077
 Planck Collaboration, Ade, P. A. R., Aghanim, N., et al. 2014, *A&A*, 571, A1
 Rosas-Guevara, Y. M., Bower, R. G., Schaye, J., et al. 2015, *MNRAS*, 454, 1038
 Sales, L. V., Navarro, J. F., Schaye, J., et al. 2010, *MNRAS*, 409, 1541
 Sales, L. V., Navarro, J. F., Theuns, T., et al. 2012, *MNRAS*, 423, 1544
 Schawinski, K., Thomas, D., Sarzi, M., et al. 2007, *MNRAS*, 382, 1415
 Schaye, J., Crain, R. A., Bower, R. G., et al. 2015, *MNRAS*, 446, 521
 Sheth, R. K., Bernardi, M., Schechter, P. L., et al. 2003, *ApJ*, 594, 225
 Silk, J. 2005, *MNRAS*, 364, 1337
 Silk, J. & Rees, M. J. 1998, *A&A*, 331, L1
 Sohn, J., Geller, M. J., Borrow, J., & Vogelsberger, M. 2024a, *ApJ*, 974, 26
 Sohn, J., Geller, M. J., Borrow, J., & Vogelsberger, M. 2024b, *ApJ*, 964, 178
 Sohn, J., Geller, M. J., Vogelsberger, M., & Damjanov, I. 2022, *ApJ*, 931, 31
 Sohn, J., Geller, M. J., Zahid, H. J., et al. 2017a, *ApJS*, 229, 20
 Sohn, J., Zahid, H. J., & Geller, M. J. 2017b, *ApJ*, 845, 73
 Springel, V., Di Matteo, T., & Hernquist, L. 2005, *ApJ*, 620, L79
 Springel, V., White, M., & Hernquist, L. 2001, *ApJ*, 549, 681
 Utsuni, Y., Geller, M. J., Zahid, H. J., et al. 2020, *ApJ*, 900, 50
 van Uitert, E., Hoekstra, H., Franx, M., et al. 2013, *A&A*, 549, A7
 Wagner, A. Y., Bicknell, G. V., & Umemura, M. 2012, *ApJ*, 757, 136
 Wake, D. A., van Dokkum, P. G., & Franx, M. 2012, *ApJ*, 751, L44
 Weigel, A. K., Schawinski, K., & Bruderer, C. 2016, *MNRAS*, 459, 2150
 Weinberger, R., Springel, V., Pakmor, R., et al. 2018, *MNRAS*, 479, 4056
 Zahid, H. J., Geller, M. J., Fabricant, D. G., & Hwang, H. S. 2016, *ApJ*, 832, 203
 Zahid, H. J., Sohn, J., & Geller, M. J. 2018, *ApJ*, 859, 96
 Zubovas, K. & King, A. 2016, *MNRAS*, 462, 4055